1

**Supporting Information for:**

3

**Surface Charge Measurements with Scanning Ion Conductance**

**Microscopy Provides Insights into Nitrous Acid Speciation at the**

**Kaolin Mineral-Air Interface**

Cheng Zhu[1], Gargi Jagdale[1], Adrien Gandolfo[2], Kristen Alanis[1], Rebecca Abney,[2,3]

Lushan Zhou[1], David L. Bish,[1] Jonathan D. Raff[1,2,*], and Lane A. Baker[1,*]

[1]*Department of Chemistry*
*Indiana University*
*Bloomington, IN 47401*

[2]*Paul H. O'Neill School of Public & Environmental Affairs*
*Indiana University*
*Bloomington, IN 47405*

[3]*Warnell School of Forestry and Natural Resources*
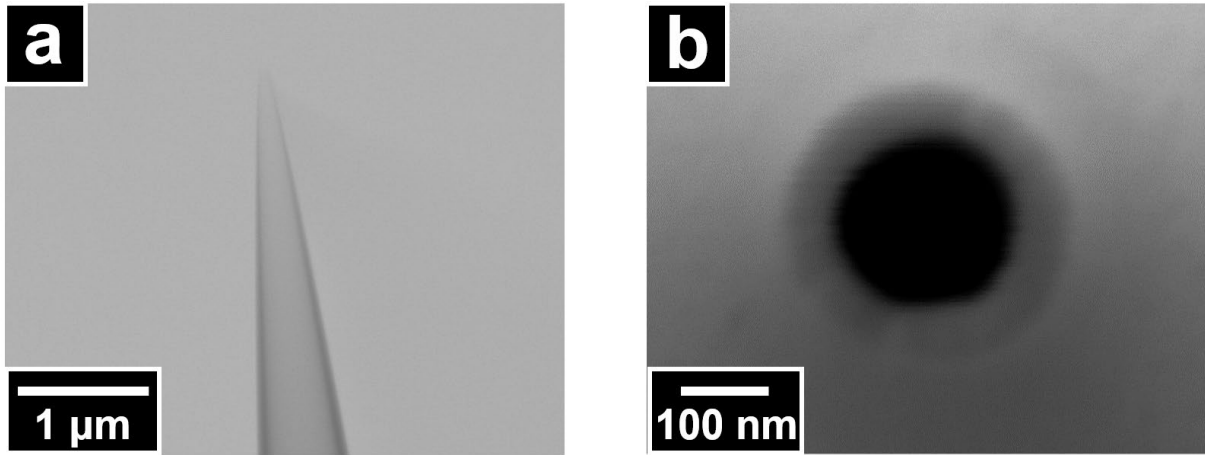*University of Georgia*
*Athens, GA 30602*

*Authors to whom correspondence should be addressed.
e-mail: lanbaker@indiana.edu; phone 812-856-1873 ; fax 812-855-8300
e-mail: jdraff@indiana.edu; phone 812-855-6525

24

# Contents

## SI-1 Election Micrographs of Nanopipettes



**Figure S1.1** Side view (**a**) and the end-on view (**b**) of a typical nanopipette used in these experiments.

## SI-2 Experimental Details of Flow Reactor Studies

**Flow Reactor Configuration**

**Figure S2.1** displays a schematic of the experimental system used to measure HONO released from nitrite reactions on clay mineral surfaces. Panel A provides an overview, and Panel B and C provide details of the sample holder located in the dashed box in Panel A.
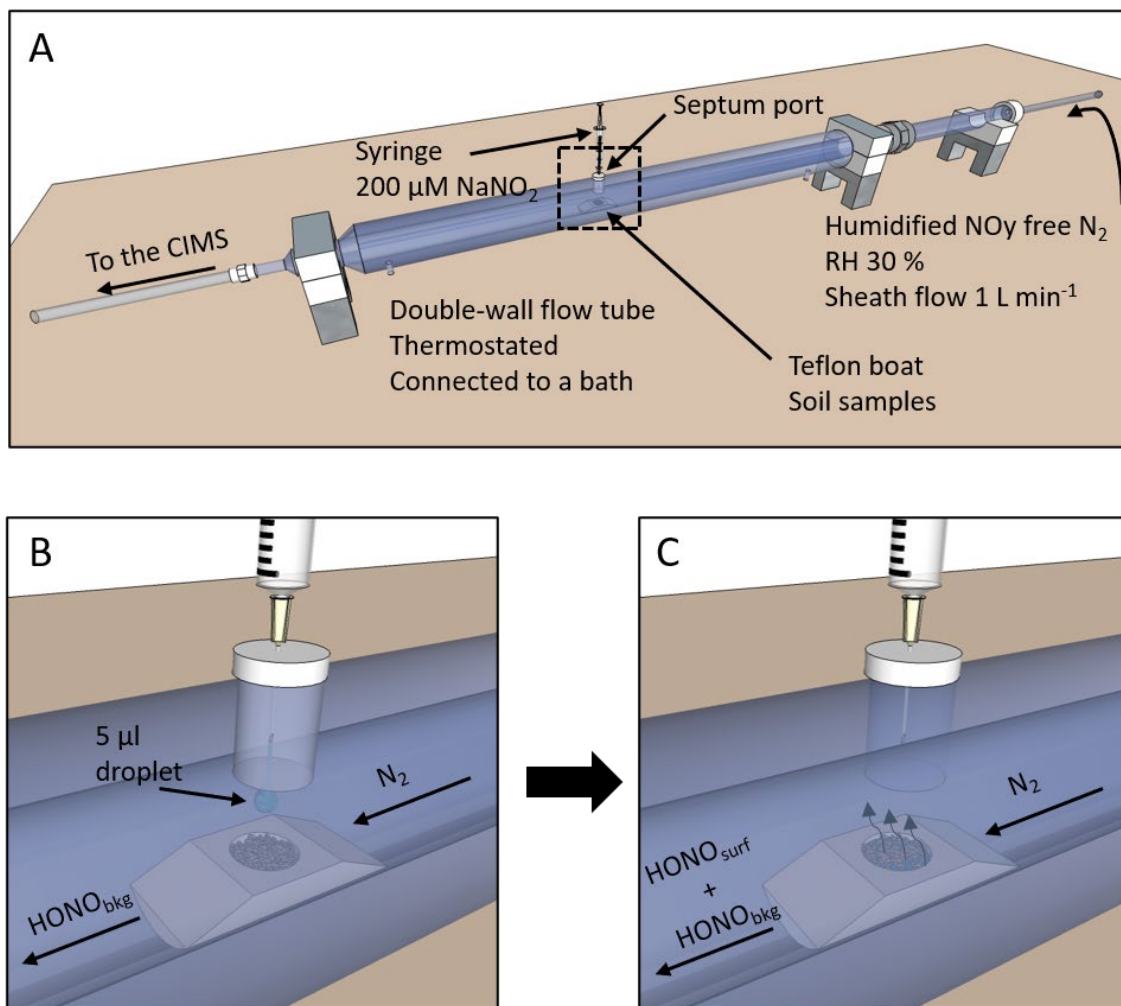


**Figure S2.1** 3D representation of the experimental setup used to study $HONO_{(g)}$ emission from nitrite reaction on mineral surfaces. Panel A shows the laminar flow tube reactor, gas in- and outlets, and the nitrite injection system (septum port and syringe). Gas exiting the flow reactor flows to the chemical ionization mass spectrometer. Panels B and C show details of the Teflon holder used to hold pure water or clay mineral samples placed underneath the injection system.

**Calibration of the Chemical Ionization Mass Spectrometer (CIMS)**

The CIMS response to HONO was calibrated in the range of 2 to 10 ppb following a method described previously.[1] Briefly, HONO is produced from the acid displacement of gaseous hydrochloric acid (HCl) flowing across a stirred bed of sodium nitrate powder at 50% relative humidity (RH). The HONO generation system, including the permeation device used to supply HCl is housed in an oven held at 55 °C. The HONO concentration in the generator outflow is monitored continuously by cavity-enhanced absorption spectroscopy (CEAS)[2] to assess the absolute mixing ratio. The generator output was 50 ± 5 ppb HONO and was subsequently diluted with humid (30% RH) high purity air to obtain the desired concentration prior to being measured by CIMS.

Following the calibration procedure described above, the CIMS sensitivity is 5442 ± 178 cps ppb$^{-1}$. A limit of detection (LOD) of 60 ppt is calculated according to the following equation:

$$[HONO]_{LOD} = [HONO]_0 + (3 \times SD_{[HONO]_0}) \qquad \textbf{Eqn S2.1}$$

where $[HONO]_0$ is the background HONO concentration measured under a flow of pure nitrogen (30% RH) for 15 min following 1 h of purging with the same carrier gas mixture; $SD_{[HONO]_0}$ is the standard deviation calculated from the same data set.

## SI-3 Finite Element Method (FEM) Simulations

To quantify the surface charge density on dickite crystals, finite-element method (FEM) simulation models were created with COMSOL Multiphysics (COMSOL, Inc.). **Figure S3.1** shows the schematic of the model. Typical dimensions of the pipette were

83    acquired from the electron micrographs. The inner radius ($r_i$) of the pipette tip opening

84    was set to 37 nm and the outer radius of the pipette ($r_o$) was set to $r_i/0.7$. The tip-to-

85    sample distance is defined as $D_{ps}$. Other parameters such as ion concentrations and

86    diffusion coefficients (taken here at infinite dilution) are shown in **Table 3.1**. The potential

87    was applied inside the pipette (B1). In contrast, the boundary on the side of the model

88    was set as ground (V = 0, B3). The boundaries highlighted in green represent the pipette

89    wall that carries a surface charge density of $\sigma_p$. It should be noted that the radius of the

90    pipette, surface charge density of the pipette, and the concentration of the solution were

91    adjusted when measuring the pH-dependent surface charge to compensate for the

92    change in the surface charge, geometry of the pipette, and the concentration change

93    resulting from the addition of acid.

94        Of note, work by Thatenhorst et. al,[3] convincingly demonstrated that steeply

95    angled surfaces result in an overestimation of the tip-sample distance, and values for the

96    maximum overestimation can be found from the product of the inner radius of the pipette

97    ($r_i$) and the slope (maximum slopes imaged here were ~2.7). For conditions here, this

98    results in a maximum of ~100 nm overestimation of the tip-sample distance, although we

99    note that this does not include possible deviations in the angle of approach of the pipette.

100    For models here, attempts to include both surface charge and sample tilt reduced model

101    symmetry and resulted in nonconvergent results. For models used here, as a first

102    approximation, no height correction for was applied.

103        After collecting the *ICD* images, the average I-V curve for basal planes was

104    calculated by averaging all the I-V curves at negative sites. Similarly, the average I-V

105    curve for edge surfaces was collected by averaging all the I-V curves at positive sites.

106    An exact value of $\sigma_p$ was first calculated by fixing the $D_{ps}$ at 2.34 μm (the retracted

107    distance used in the experiment, where the I-V is independent from the surface charge

108    on sample surfaces) and then changing the $\sigma_p$ until the resultant I-V curve matched the

109    retracted I-V curve measured in the experiment.
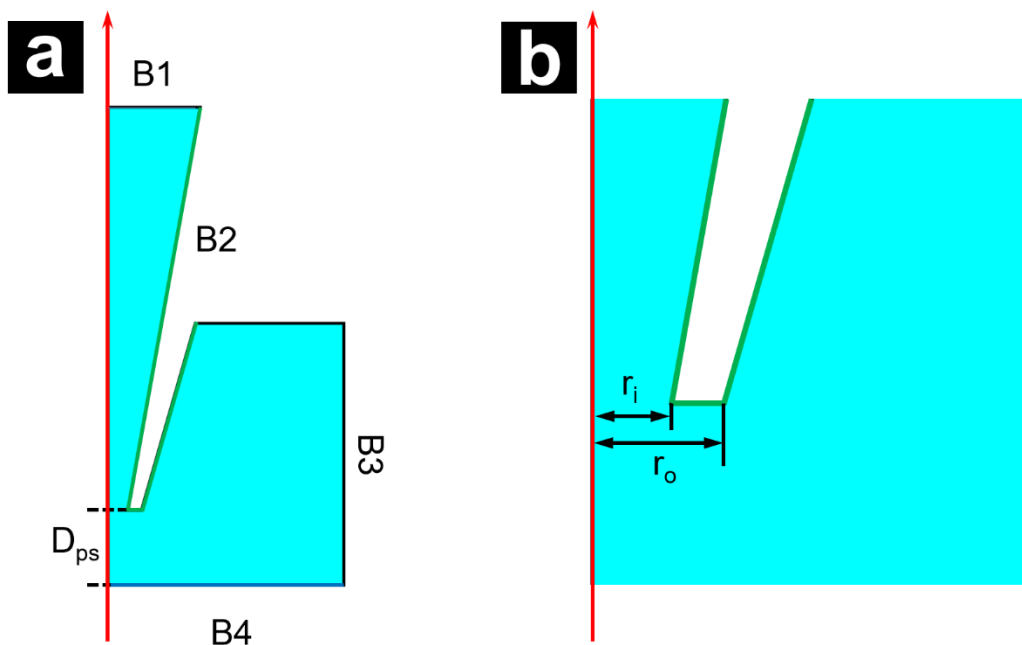


110    **Figure S3.1** (**a**) Schematic of the model created with COMSOL Multiphysics. The
111    potential was applied inside the pipette (B1) and the boundary on the side of the model
112    was set as ground (B3). The green lines highlight the boundaries that carry a surface
113    charge on the pipette (B2). The sample surface charge is highlighted in blue (B4). (**b**) At
114    the highlighted areas near the tip opening, the inner and outer radius of the pipette was
115    set as $r_i$ and $r_o$, respectively.

116    After resolving the surface charge of the pipette, $D_{ps}$ was then reduced to a small

117    value which is close to the outer radius of the pipette used in the experiment. Both the

118    $D_{ps}$ and the surface charge on samples ($\sigma_s$) were then adjusted in simulations until the

119    resultant I-V curve matched the extended I-V curve measured in the experiment.

120    Reducing $D_{ps}$ typically reduces the current magnitude of I-V at both positive potentials

121    and negative potentials. In contrast, increasing $\sigma_s$ results in an increase of current at

122 positive potentials and a decrease in current at negative potentials. Only one of the $D_{ps}$

123 and $\sigma_s$ combinations will result in an I-V that exactly matches that collected in the

124 experiment.

125 **Table S3.1** Common Parameters used in the FEM Simulation

| Parameter | Typical values | Description |
|---|---|---|
| $r_i$ | 34 nm | Inner radius of the pipette |
| $r_o$ | $r_i/0.7$ | Outer radius of the pipette |
| $C_{K^+}$ | 100 mM | Concentration of potassium ions |
| $C_{Cl^-}$ | 100 mM | Concentration of chloride ions |
| $C_{H^+}$ | 10 µM | Concentration of protons |
| $D_{K^+}$ | $1.957 \times 10^{-9}$ m$^2$/s | Diffusion coefficient of potassium ions |
| $D_{Cl^-}$ | $2.032 \times 10^{-9}$ m$^2$/s | Diffusion coefficient of chloride ions |
| $D_{H^+}$ | $9.320 \times 10^{-9}$ m$^2$/s | Diffusion coefficient of protons |
| V+ | 600 mV | The maximum positive potential applied during I-V measurement |
| V- | -600 mV | The maximum negative potential applied during I-V measurement |
| $\alpha_i$ | 5.64 ° | Inner half cone angle of the pipette |
| $\alpha_o$ | $1.35 \times \alpha_i$ | Outer half cone angle of the pipette |

126

127 **Table S3.2** Simulation Parameters and Results for Figure 4

| pH of bulk solution | $r_i$ | $\sigma_p$ | $D_{ps}$ | $\sigma_s$ |
|---|---|---|---|---|
| 5 | 32.54 nm | -7.48 mC/m$^2$ | 52.7 nm | 3 mC/m$^2$ |
| 4 | 33.22 nm | -5.00 mC/m$^2$ | 53.0 nm | 10 mC/m$^2$ |
| 3 | 34.08 nm | -2.84 mC/m$^2$ | 53.4 nm | 31 mC/m$^2$ |

128

129

130 **Table S3.3** Simulation Parameters and Results for Figure 3

| pH of bulk solution | $r_i$ | $\sigma_p$ | $D_{ps}$ | $\sigma_s$ |
|:---:|:---:|:---:|:---:|:---:|
| 5 | 25.55 nm | -14.25 mC/m$^2$ | 24.5 nm | -132 mC/m$^2$ |
| 4 | 26.43 nm | -8.33 mC/m$^2$ | 26.1 nm | -133 mC/m$^2$ |
| 3 | 27.31 nm | -3.92 mC/m$^2$ | 30.5 nm | -135 mC/m$^2$ |

131

## SI-4 Characterization of Dickite Samples

### Structure of Kaolin Group Minerals

134       Kaolin group minerals, $Al_2Si_2O_5(OH)_4$, are among the most abundant clay minerals

135  in soil. The structure of the kaolin minerals, kaolinite, dickite, and nacrite have already

136  been well investigated previously with multiple techniques, including X-ray and neutron

137  diffraction,[4] X-ray absorption spectroscopy,[5, 6] Fourier-transform infrared spectroscopy

138  (FTIR),[4, 7-9] atomic force microscopy (AFM),[10-12] nuclear magnetic resonance (NMR)[13]

139  and electron microscopy (EM).[14] All of these techniques demonstrate that kaolin group

140  minerals are composed of a periodic layered structure consisting of a layer of $SiO_4$

141  tetrahedra (T, siloxane) linked to a sheet of aluminum (hydr)oxide octahedra (O, gibbsite)

142  via shared oxygen and hydroxide groups (**Figure S4.1**). The basic TO structure is

143  repeated in space with hydrogen bonds holding together neighboring TO layers.

144  Depending on the stacking of individual TO layers the kaolin group minerals are further

145  classified into kaolinite, nacrite, and dickite.[15]  Dickite was used in these studies as a

146  proxy for all of the kaolin group minerals because it is readily available in well-ordered

147  macroscopic crystals. Dickite samples used for this study were characterized by scanning

148    electron microscopy (FEI Quanta-FEG, Hillsboro, OR). Selected micrographs of dickite

149    are shown in **Figure S4.2** and **S4.3**.

150
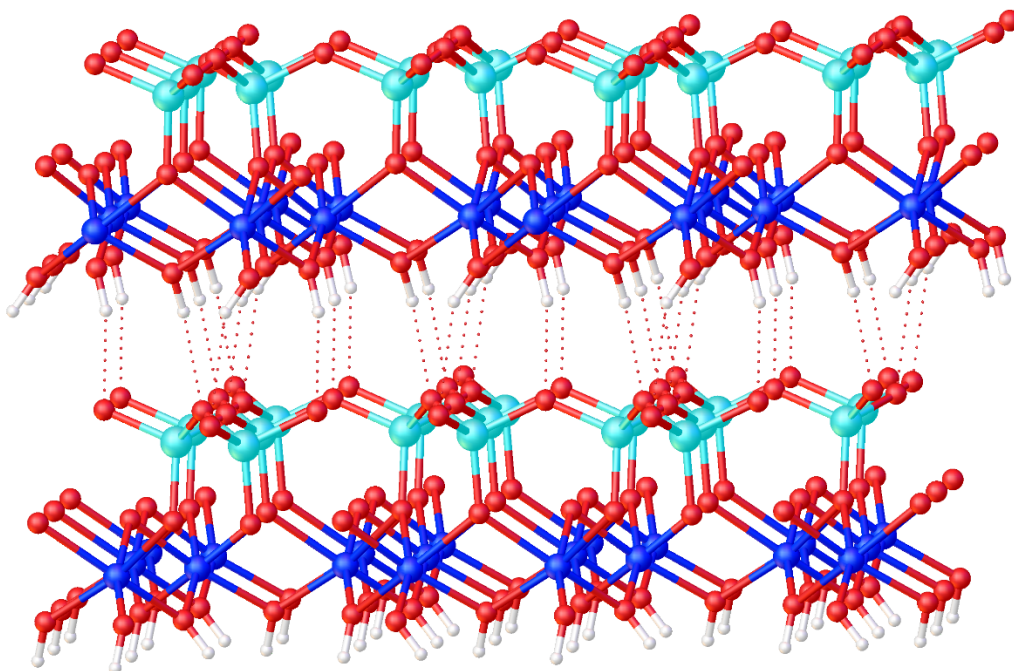


151

152    **Figure S4.1** The typical structure of kaolin group minerals. Each silicon is surrounded by
153    four oxygens, which forms an extended tetrahedral silica sheet.  Four hydroxide groups
154    and two oxygens surround each aluminum ion to form an extended octahedral gibbsite
155    sheet. Silica and gibbsite sheets are bonded together by shared oxygens and hydroxide
156    groups. Repeated silica-gibbsite units held together by interlayer hydrogen bonds to yield
157    a layered structure.  Color code:  Cyan = Si; Red = O, White = H; Blue = Al.
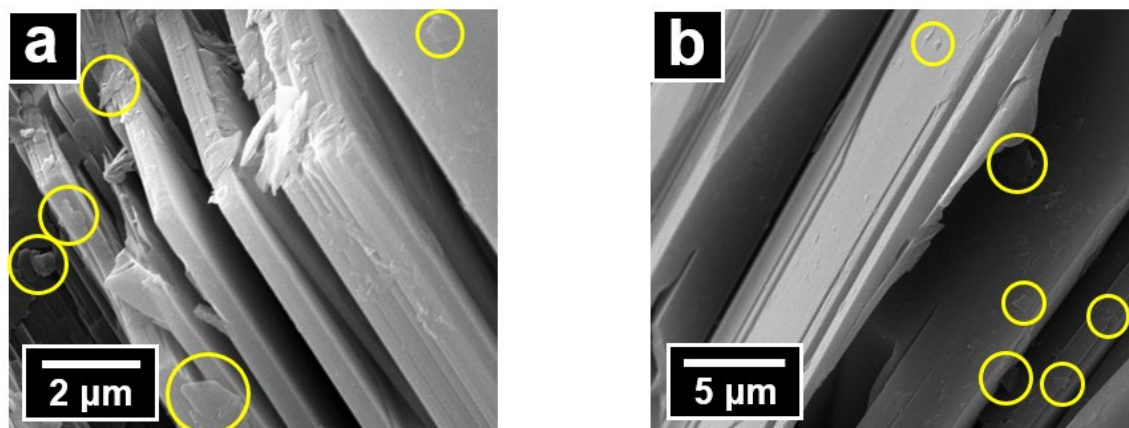
158

159
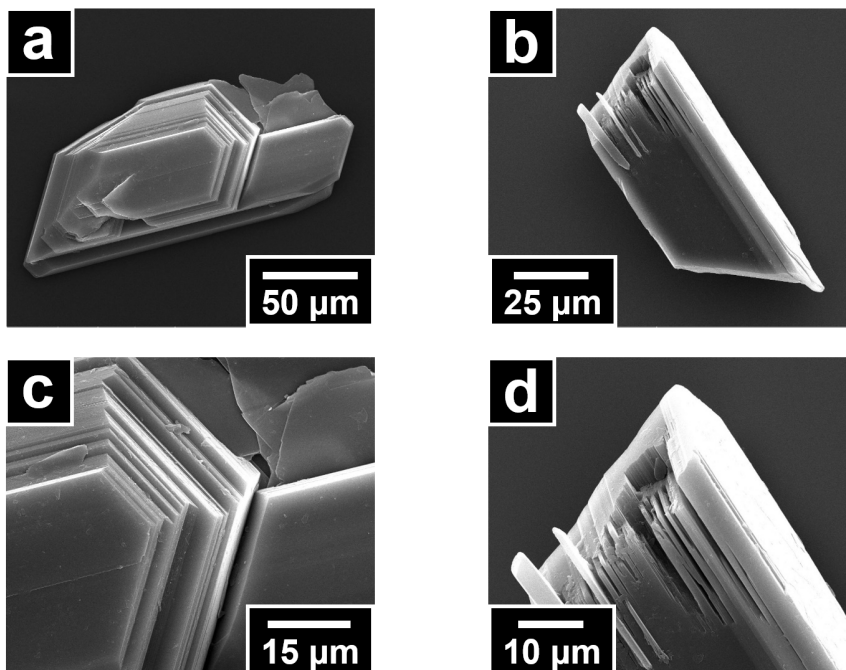
**Figure S4.2** Scanning electron micrographs of dickite crystals in various orientations. In (**a**) and (**c**) the basal plane is in contact with the substrate whereas in (**b**) and (**d**) edge surfaces contact the substrate.

163



164

**Figure S4.3** Scanning electron micrographs of dickite crystals. Yellow circles highlight numerous small dickite flakes adhered to the dickite crystals.

167

**Characterizing and Orienting Individual Dickite Crystals for SICM Analysis**

168

169       Single crystals of dickite were selected under a polarizing microscope and

170 mounted without adhesives or oil to avoid surface contamination. They were placed on

171 MiTeGenTM Kapton micro loops or micro grippers and mounted on a Bruker Venture D8

172 diffractometer equipped with a PhotonIII detector for data collection at 297(2) K.

173       X-ray diffraction data collection was carried out using an I$\mu$S 3.0, Incoatec source

174 and Mo K$\alpha$ radiation (graphite monochromator) with a frame time of 0.5, 0.75, or 1 second

175 and a detector distance of 40.00 mm. Data were measured to a resolution of 0.71 Å with

176 a redundancy of 4. Three or five major sections of frames were collected with 1º $\omega$ and $\phi$

177 scans. An additional fast scan was collected to obtain accurate intensities for a few high-

178 intensity reflections. The frames were integrated with the Bruker SAINT software

179 package[16] using a narrow-frame algorithm, and data were scaled and corrected for

180 absorption effects using the Multi-Scan method (SADABS[17]).

181       Space group Cc was determined based on intensity statistics and systematic

182 absences, consistent with the published structure. The structure was solved and refined

183 using the SHELX suite of programs.[18, 19] An intrinsic-methods solution was calculated,

184 which provided all non-hydrogen atoms from the E-map. Full-matrix least squares /

185 difference Fourier cycles were performed, by which hydrogen atoms were located. All

186 non-hydrogen atoms were refined with anisotropic displacement parameters. The

187 hydrogen atoms were refined freely with isotropic displacement parameters. The final

188 anisotropic full-matrix least-squares refinement on $F^2$ resulted in low R values and a near-

189 featureless difference map. Flack parameters were calculated from anomalous dispersion.
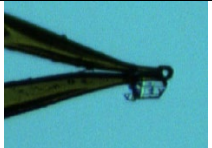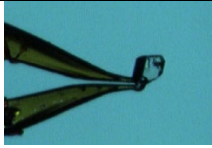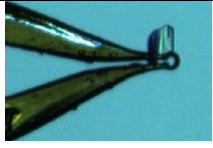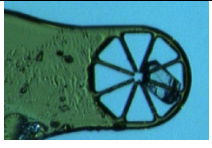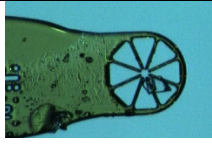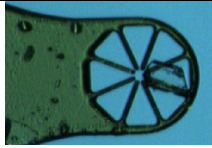
190   The face index of the crystals was determined to relate Miller planes (0 0 1) and (0 0 -1)

191   to the orientation of the TO layers of dickite, comprised of Si-O tetrahedra on one side

192   and Al-O,OH octahedra on the other side. Subsequently, the crystals were transferred

193   with known orientation onto the PDMS substrate for further investigation.

194       Additional measurement parameters and refinement results are summarized

195   below. Images of the crystal, the asymmetric unit, and the unit cell are shown as well.

196   CIFs are included as supplemental information.

197

198

**Table S4.1** Crystallographic measurement parameters and refinement results for oriented dickite crystals and their corresponding charge maps.

| Sample # | 21061 | 21062 | 21063 | 21068 | 21069 | 21070 |
|---|---|---|---|---|---|---|
| Emp. Formula, formula weight | $Al_2H_3O_9Si_2$, 257.16 g/mol | | | | | |
| Crystal color, shape | colorless plate | | | | | |
| Crystal size in mm³ | 0.129×0.098×0.031 | 0.251×0.108×0.080 | 0.143×0.126×0.053 | 0.265×0.126×0.054 | 0.194×0.134×0.055 | 0.192×0.125×0.061 |
| Crystal image |  |  |  |  |  |  |
| Crystal system, space group, Z | Monoclinic, Cc, 4 | | | | | |
| Unit cell dimensions: | 5.1481(5) | 5.1422(4) | 5.1466(7) | 5.1463(4) | 5.1478(2) | 5.1456(3) |
| a, b, c in Å and β in ° | 8.9376(10) | 8.9294(7) | 8.9329(10) | 8.9331(5) | 8.9352(4) | 8.9331(5) |
| | 14.4234(17) | 14.4146(10) | 14.4141(18) | 14.4149(11) | 14.4183(7) | 14.4130(10) |
| | 96.751(3) | 96.753(3) | 96.723(4) | 96.741(3) | 96.719(2) | 96.739(3) |
| Volume in Å³ | 659.04(12) | 657.28(9) | 658.12(14) | 658.11(8) | 658.64(5) | 657.93(7) |
| Density (calculated) in Mg/m³ | 2.592 | 2.599 | 2.595 | 2.596 | 2.593 | 2.596 |
| Absorption coefficient in mm⁻¹ | 0.833 | 0.835 | 0.834 | 0.834 | 0.833 | 0.834 |
| | | | | | | |
| **Data collection** | | | | | | |
| θ range in ° | 2.844 to 30.039 | 2.846 to 30.064 | 2.846 to 30.023 | 2.846 to 30.532 | 2.845 to 30.046 | 4.563 to 30.023 |
| Index ranges | -6<=h<=7, -12<=k<=12, -20<=l<=20 | -7<=h<=7, -12<=k<=12, -19<=l<=20 | -7<=h<=7, -12<=k<=10, -20<=l<=20 | -7<=h<=7, -12<=k<=12, -20<=l<=20 | -7<=h<=7, -12<=k<=12, -20<=l<=18 | -7<=h<=7, -11<=k<=12, -20<=l<=20 |
| Reflections collected | 6838 | 8013 | 6500 | 7268 | 7072 | 6920 |
| Independent reflections | 1836, $R_{int}$ = 0.1069 | 1858, $R_{int}$ = 0.0536 | 1918, $R_{int}$ = 0.1271 | 1851, $R_{int}$ = 0.0388 | 1807, $R_{int}$ = 0.0460 | 1853, $R_{int}$ = 0.0409 |
| Observed Reflections | 1232 | 1632 | 1192 | 1657 | 1636 | 1682 |
| Completeness to θ = 25.242° in % | 100.0 | 99.8 | 99.8 | 99.8 | 99.8 | 99.5 |

**Solution and Refinement**

| Absorption correction | Semi-empirical from equivalents | | | | | |
|---|---|---|---|---|---|---|
| Max. and min. transmission | 0.7460 and 0.6818 | 0.7460 and 0.6837 | 0.7460 and 0.6156 | 0.7460 and 0.6818 | 0.7460 and 0.6620 | 0.7460 and 0.6506 |
| A for weighting scheme $w=[\sigma^2 Fo^2 + A[(Fo^2 + 2Fc^2)/3]^2 + ]^{-1}$, | 0.0309 | 0.0301 | 0.0319 | 0.0488 | 0.0381 | 0.0323 |
| Data / restraints / parameters | 1836 / 2 / 130 | 1858 / 2 / 130 | 1918 / 2 / 130 | 1851 / 2 / 130 | 1807 / 2 / 130 | 1853 / 2 / 130 |
| Goodness-of-fit on $F^2$ | 1.003 | 1.068 | 0.998 | 1.139 | 1.086 | 1.043 |
| R indices [I>2$\sigma$(I)], R1 and wR2 | 0.0495 and 0.0756 | 0.0290 and 0.0592 | 0.0619 and 0.0991 | 0.0351 and 0.0837 | 0.0327 and 0.0713 | 0.0296 and 0.0624 |
| R indices (all data), R1 and wR2 | 0.1052 and 0.0874 | 0.0406 and 0.0618 | 0.1257 and 0.1177 | 0.0432 and 0.0862 | 0.0398 and 0.0744 | 0.0357 and 0.0647 |
| Flack parameter | -0.08(17) | 0.04(8) | -0.5(3) | -0.01(8) | 0.01(10) | 0.05(9) |
| Largest diff. peak and hole in e/Å$^{-3}$ | 0.589 and -0.626 | 0.378 and -0.477 | 0.630 and -0.684 | 0.579 and -0.579 | 0.539 and -0.558 | 0.473 and -0.394 |
| Composition of (0 0 1) face | Si-O tetrahedra | Al-O, OH octrahedra | Si-O tetrahedra | Al-O, OH octrahedra | Si-O tetrahedra | Al-O, OH octrahedra |
| Optical Microscope image of dickite crystal on SICM stage |  |  |  |  |  |  |
| SICM topography (16 by 15.6 µm) |  |  |  |  |  |  |
| ICD map of (0 0 1) face (16 by 15.6 µm) |  |  |  |  |  |  |
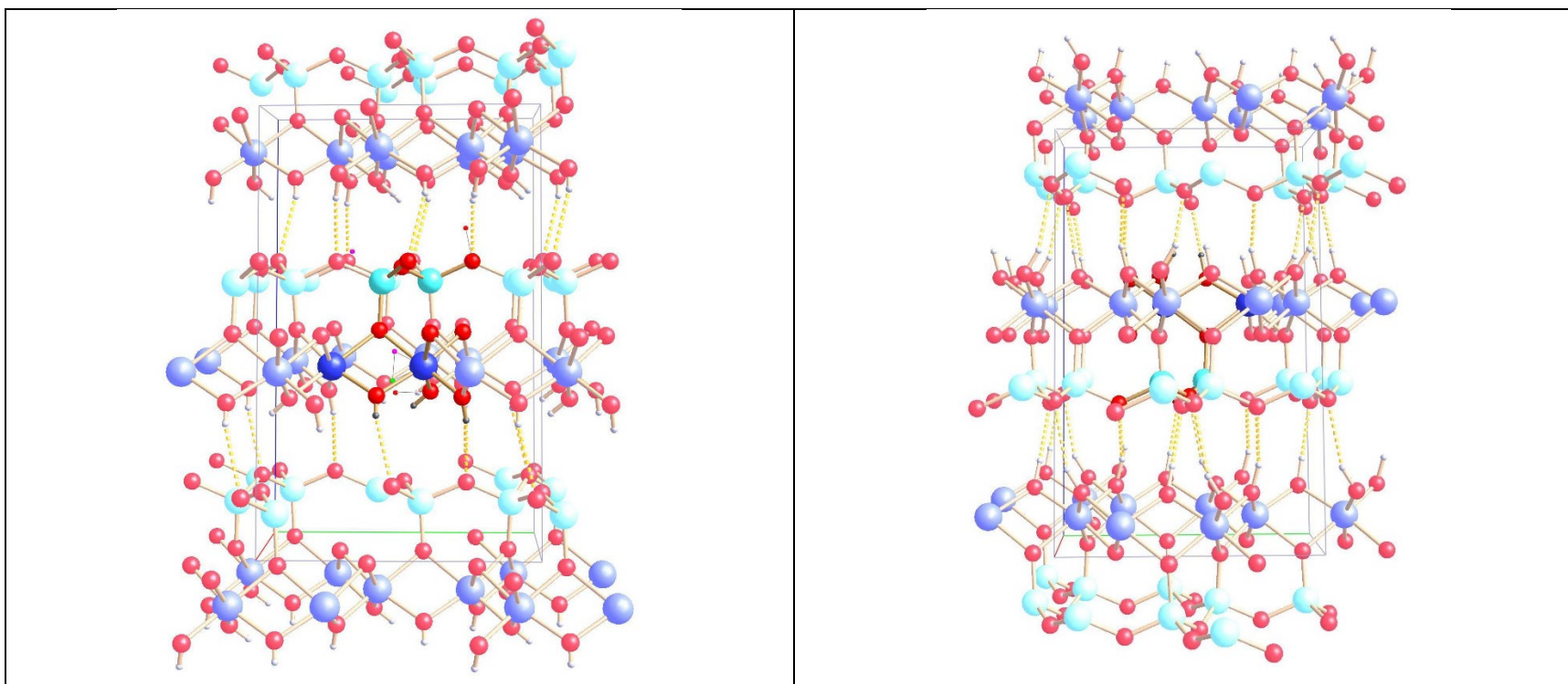
**Figure S4.4  Left:** Packing and unit cell of crystal 21061, representative of 21063 and 21069. **Right:** Packing and unit cell of crystal 21062, representative of 21068 and 21070. View along the crystallographic *a* axis.
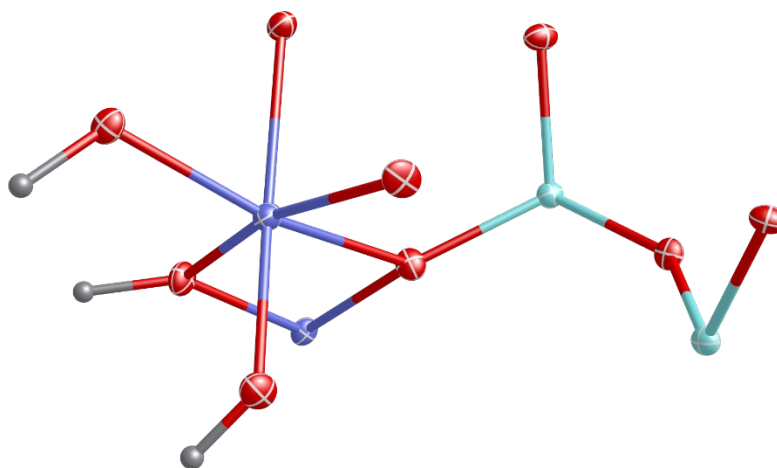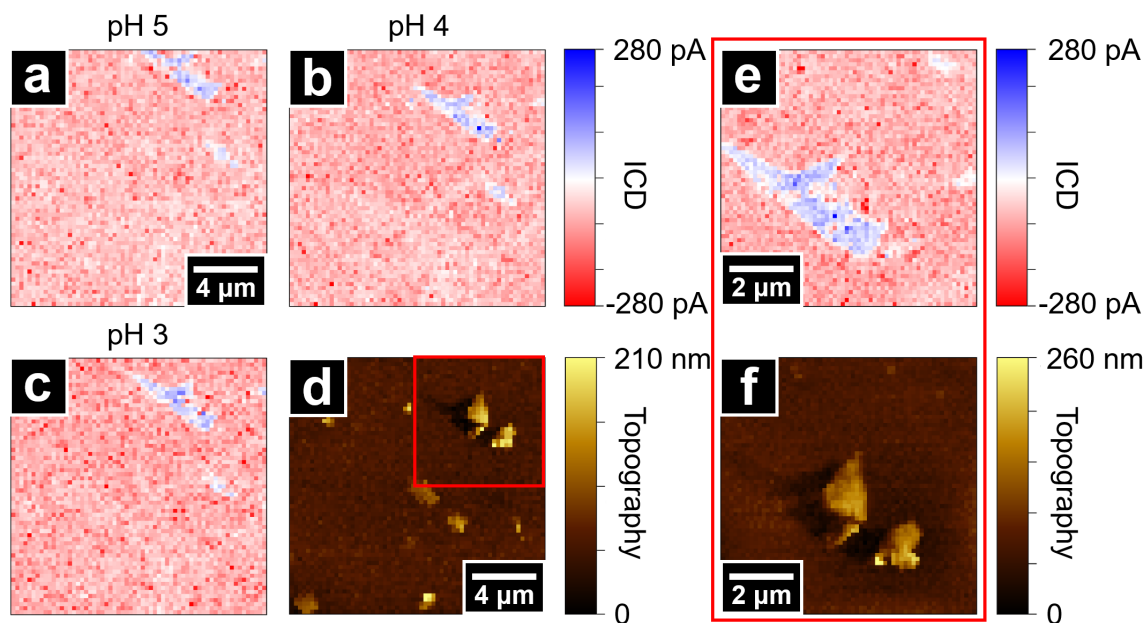
**Figure S4.5** Asymmetric unit of crystal 21061, which is representative of all other crystals.

Displacement ellipsoids are at 50% probability.

# SI-5 Topography and Surface Charge Images of the Basal Plane of a Dickite Crystal



**Figure S5.1** Surface charge images of the basal plane of a dickite crystal at pH 5 (**a**), 4 (**b**), and 3 (**c**) and the topography of the scan area (**d**). These images show a defect (pit) on the surface exposed a positively charged surface underneath the surface. High-resolution surface charge (**e**) and topography (**f**) images of the area highlighted by the red square in (**d**).

## SI-6 Secondary Ion Mass Spectrometry Images of Dickite Crystals
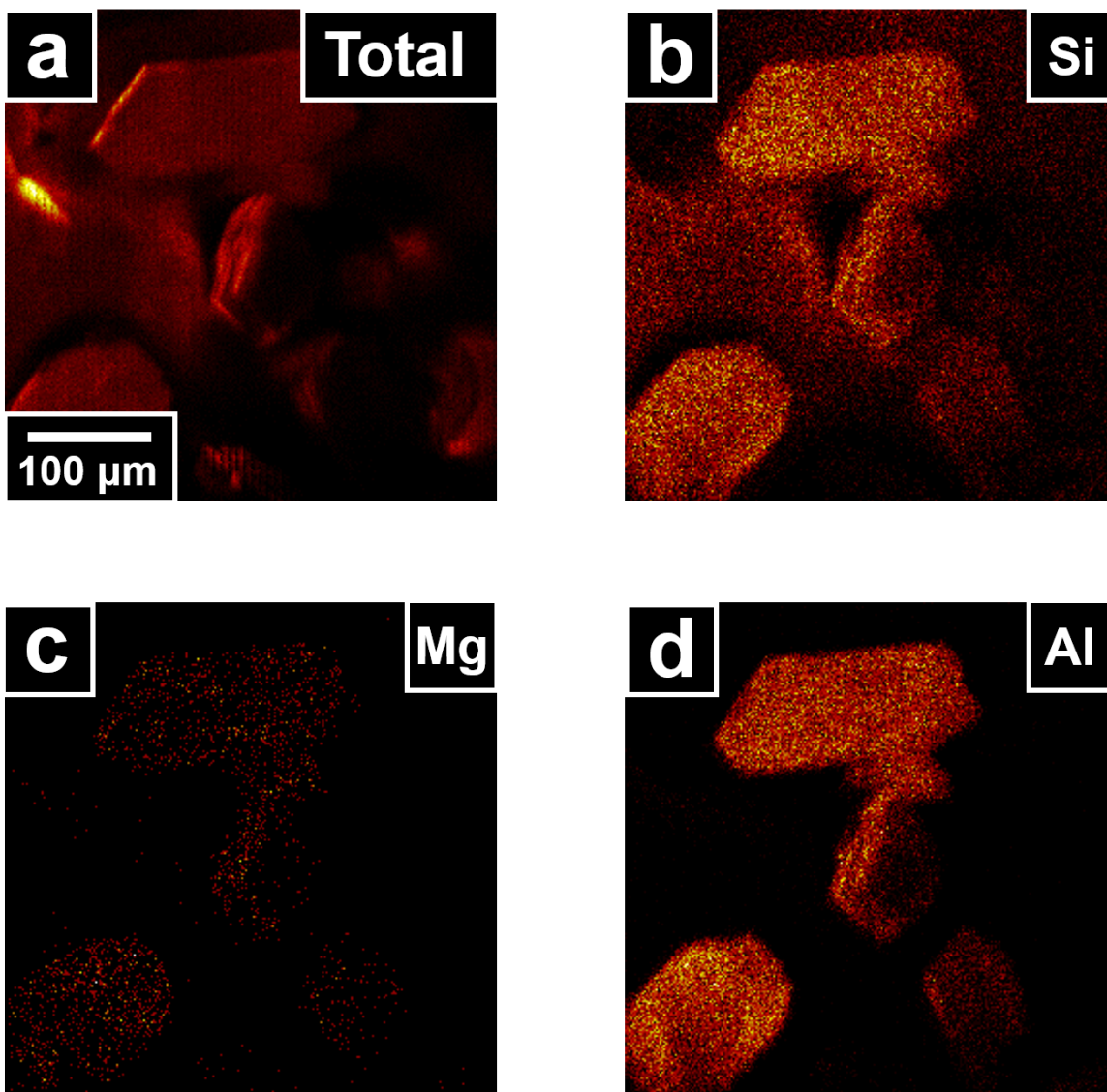


**Figure S6.1** Secondary ion mass spectrometry images of dickite crystals. As indicated by the similar intensity shown in (**b**) and (**d**), dickite crystals are composed of an almost equal amount of silicon and aluminum; magnesium appears as a minor component of the surface in (**c**).

# SI-7 Additional SICM Results of the Interactions between Malonate and Dickite Crystals
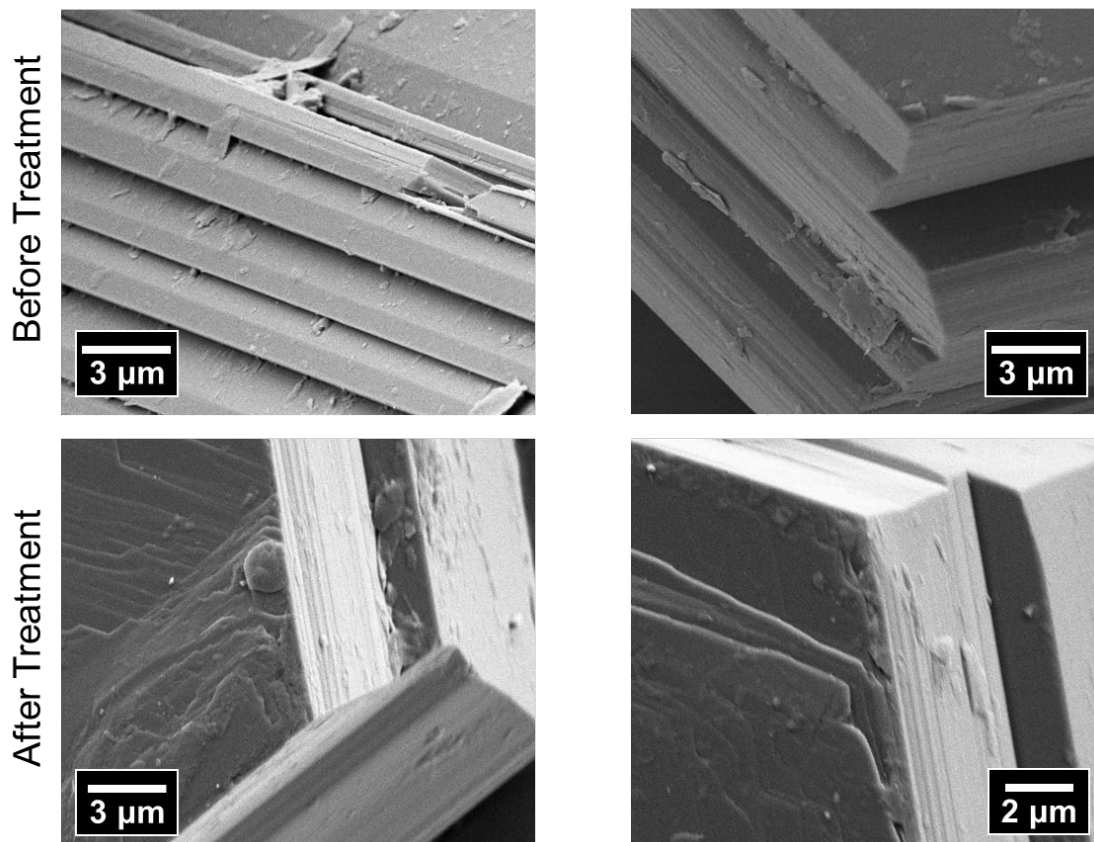


**Figure S7.1** Electron micrographs of dickite particles before (top) after (bottom) immersion in 100 mM KCl and 10 mM potassium malonate overnight. After immersion, adsorbates appear and step edges are less well defined.
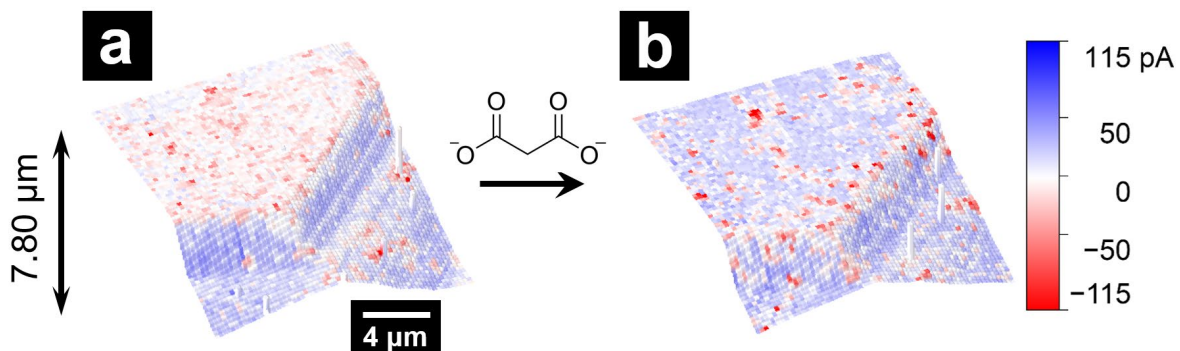
**Figure S7.2** (a) Combined topography and surface charge image of a dickite crystal in 100 mM KCl solution. (b) The addition of malonate turned the negative surface charge into positive on basal planes. Image (b) is recorded 105 minutes after image (a), solution pH = 5.
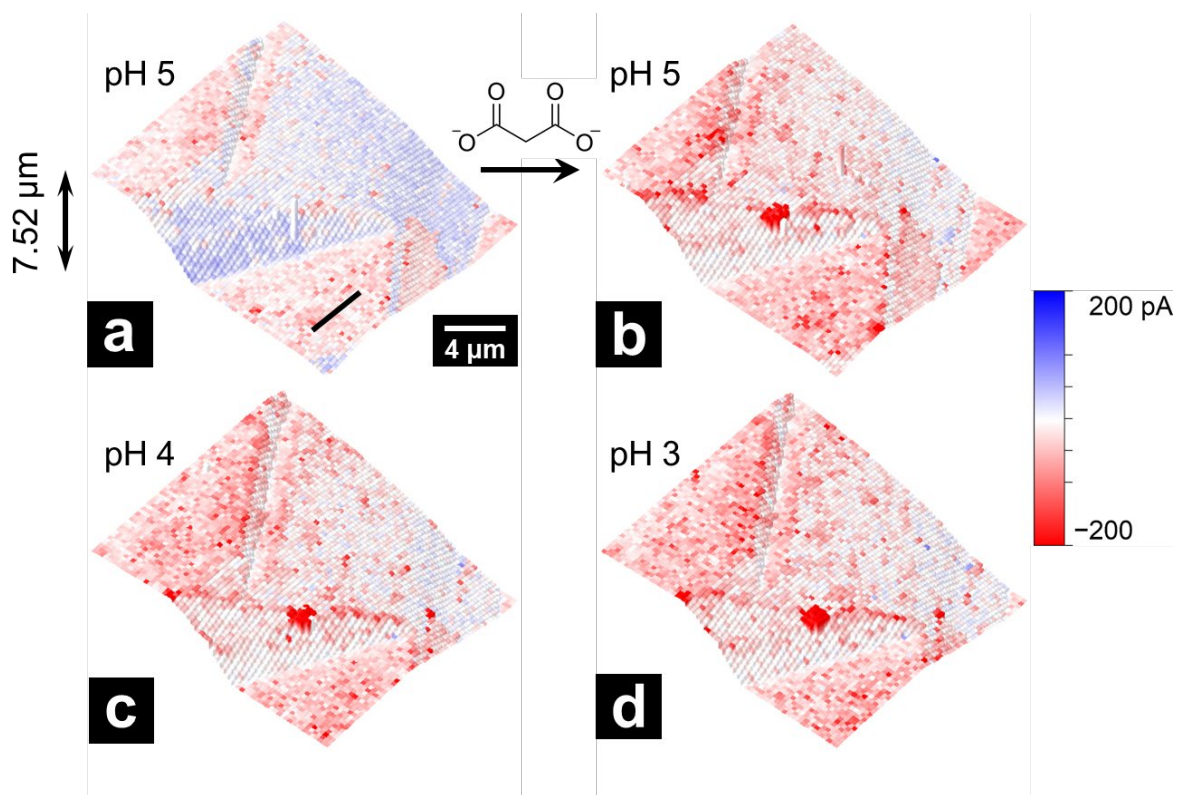
**Figure S7.3** Combined topography and surface charge images of a dickite crystal before (**a**) and after (**b**) the addition of malonate. Upon lowering the pH (**c, d**), the addition of acid does not change the apparent surface charge further.  Images recorded in succession, with image acquisition time ca. 135 minutes.  Image (**a**) recorded prior to addition of malonate.

## SI-8 HONO Emission Flux Estimation

Chemical ionization mass spectrometry was used to quantify the amount of HONO$_{(g)}$ emitted from the surface of clay mineral substrates upon addition of 1 nmol NO$_2^-$. A dilution step was applied to compensate for the CIMS inlet flow (3500 ml min$^{-1}$) compared to the flow tube outflow (1000 ml min$^{-1}$). Before each experiment, 5 to 10 consecutive measurements of both flow, reactor outflow, and dilution flow was performed to estimate the dilution correction factor. The emission flux was calculated from **Eqn S8.1**:

$$F_{HONO} = \frac{[HONO]_{corr} \times c \times Q}{A \times m \times 10000} \qquad \textbf{Eqn S8.1}$$

where [HONO]$_{corr}$ is the HONO mixing ratio corrected for dilution in ppt, $c$ is a conversion factor from ppt to molecule cm$^{-3}$, $Q$, the sheath flow running in the flow tube (cm$^3\cdot$s$^{-1}$), $A$ is the specific surface area (as presented in **Table S9.3**) in g$\cdot$m$^{-2}$ and $m$ is the mass sample in g. The specific surface area of the clay minerals was determined using a gravimetric method that measures the adsorption of vapor-phase ethylene glycol monoethyl ether (EGME), which probes both the external surface and sub-nanometer pores of phyllosilicates.[20] Emission flux is also presented as a function of the geometric surface area in **Figure S8.2**. In this case, the numerator in **Eqn S2** is replaced by the geometric surface area of exposed sample surface, 1.327 cm$^{2,}$ in our experimental setup. HONO flux calculations presented in this study are corrected for background levels of HONO present in the system, as defined by the average HONO mixing ratio determined five minutes before nitrite injection.

Before the nitrite solution injection (**Figure S2.1b**), the $HONO_{bkg}$ signal recorded was stable at low levels, as presented in **Figure S8.1** (light grey area). In this figure, the mean HONO signal is 801 ± 181 cps, which is typical of the background level observed in all experiments. Following nitrite injection (**Figure S2.1c**), the CIMS measured the sum of the $HONO_{bkg}$ and the HONO released into the gas phase from the surface ($HONO_{surf}$) (**Figure S8.1**, grey area).
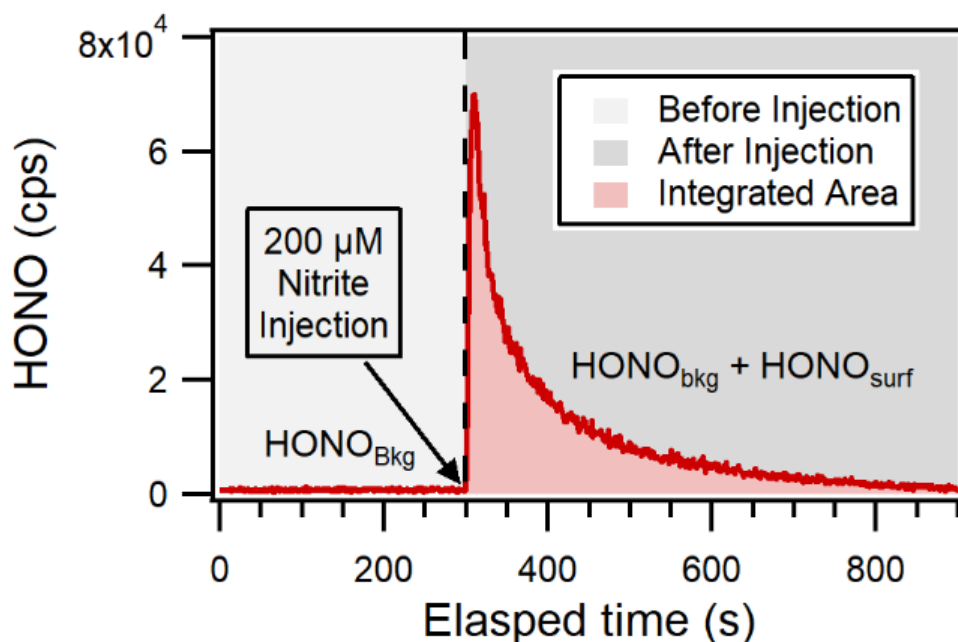


**Figure S8.1** Experimental profile of the nitrite reactivity on the mineral surface forming HONO. Raw HONO signal is express in counts per second (cps) corrected for dilution as recorded by the CIMS. The light grey and grey areas represent the HONO measurements before and after nitrite injection, respectively. The light red area represents the HONO integrated area surface area presented in titration figures.
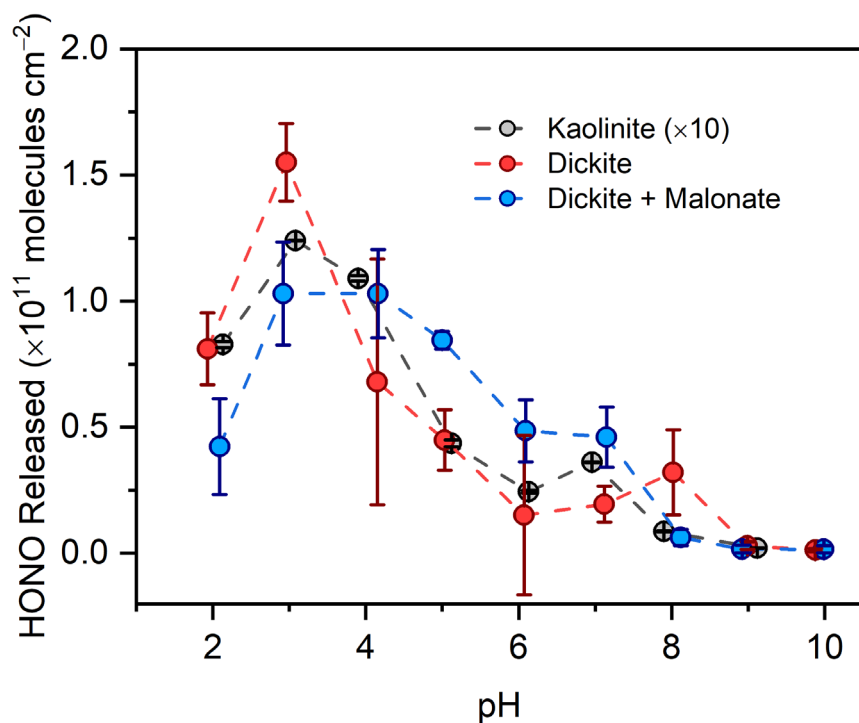
**Figure S8.2** The pH profile for the integrated HONO emission flux stemming from the addition of 1 nmol of nitrite on clay mineral surfaces. The amount of HONO emitted is relative to the geometric surface area of the sample holder, rather than the specific surface area used to display the data in Figure 6. Dotted lines are guides for the eye, and the error bars represent the 95% confidence interval of the mean of three replicate measurements. Note that amount of HONO released from kaolinite has been multiplied by 10 for clarity.
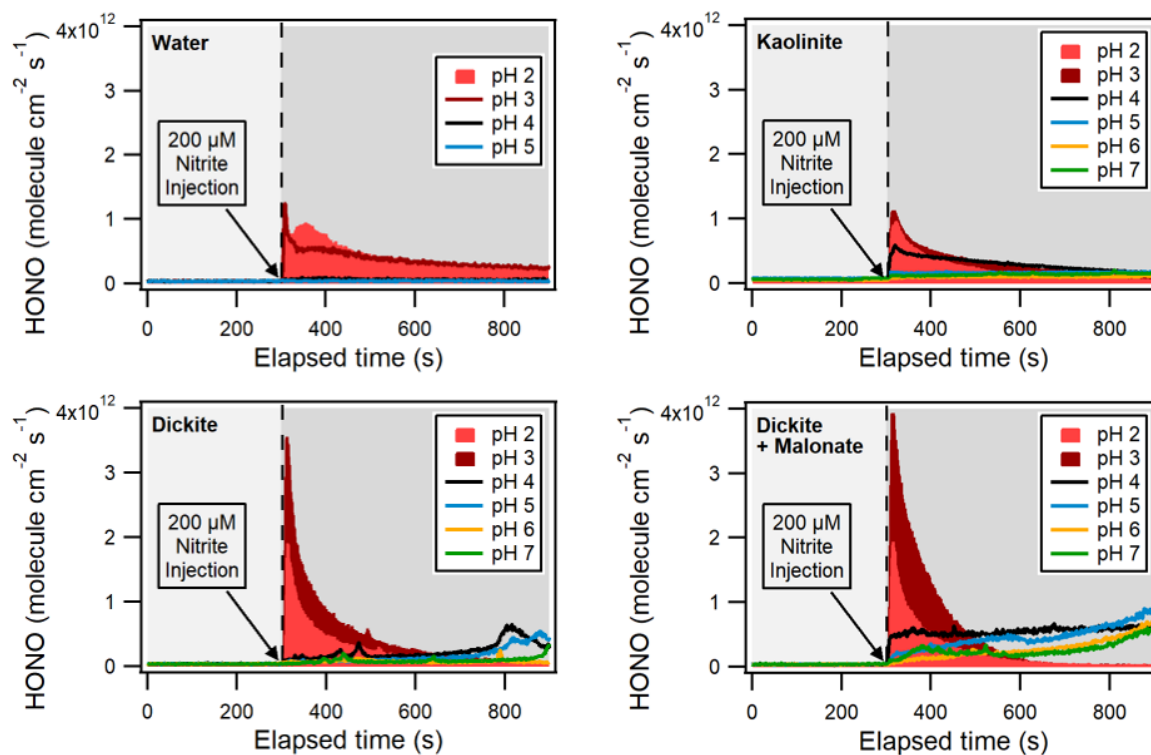
**Figure S8.3** Time series of the HONO emitted from pH adjusted systems (normalized to the geometric surface area of the substrate). The traces represent the means of triplicate experiments. Statistical standard deviation is not shown for clarity purposes. The mean statistical standard deviations are 17–33 %, 12–39 %, 18–49 %, and 16–26 % for the water, kaolinite, dickite, and dickite + malonate systems, respectively.

## SI-9 Dissolution Studies and ICP-MS analysis of the bulk solution

Soluble reaction products stemming from surface complexation of malonate on dickite surfaces were analyzed as follows. Dickite crystals were immersed in the malonate-containing solutions overnight, and the bulk solutions were subsequently analyzed with inductively coupled plasma-mass spectrometry (ICP-MS). Details of the experiment conditions are listed in **Table S9.1**. The samples are classified into two groups. The first group consists of samples 1 and 2, which are similar to the SICM experiment condition, in which several tens of dickite crystals were transferred onto a PDMS coated Petri dish and immersed in the same solution used in SICM measurements. The second group consists of samples 3 and 4, which are prepared by immersing dickite crystals in a more concentrated malonate solution.

To prepare samples for ICPMS analysis, each sample vial containing the malonate extract solution was submerged in a water bath at 75 °C and dried under a gentle flow of ultrapure $N_2$ (Airgas, 5.0), delivered by a needle above the solution. The resulting dry samples were then diluted in 2% nitric acid. Nitric acid was vacuum distilled to ensure highest purity, and then diluted with DI water to obtain the desired concentration. Samples were then analyzed on an Agilent 7700 inductively coupled plasma mass spectrometer (ICP-MS).  Results of ICP-MS analyses are summarized in **Table S9.2**.

**Table S9.1 Experiment Conditions for ICP-MS Analysis**

| Sample number | Mass of dickite crystals | Solution Composition |
|---|---|---|
| 1 | <1 mg | 100 mM KCl + 10 mM malonic acid (pH adjusted to 7 with 1M KOH) |
| 2 | <1 mg | 100 mM KCl + 10 mM malonic acid (pH adjusted to 5 with 1M KOH) |
| 3 | 22.8 mg | 300 mM malonic acid (pH adjusted to 5 with 1M KOH) |
| 4 | 26.2 mg | 1 M malonic acid (pH adjusted to 5 with 1M KOH) |

**Table S9.2 Element Concentration in Solutions**

| Element Concentration (ppb) | Dilution Ratio | Sample 1 | Sample 2 | Sample 3 | Sample 4 |
|---|---|---|---|---|---|
| Na (ppb) | 10 | 3151 | 3338 | 7249 | 13846 |
| Mg (ppb) | 10 | 25 | 29 | 33 | 32 |
| Al (ppb) | 10 | 392 | 339 | 346 | 251 |
| Si (ppb) | 1000 | 83157 | 82551 | 91969 | 143214 |
| K (ppb) | 1000 | 1772583 | 1822373 | 14142257 | 17009670 |
| Ca (ppb) | 10 | 0 | 0 | 0 | 0 |

**Table S9.3 Specific Surface Area of Clay Minerals Measured using EGME Method**

| | EGME SA ($m^2 g^{-1}$) (± 1 SD) | Number of samples |
|---|---|---|
| Kaolinite | 28.2 (± 4.4) | n = 6 |
| Dickite | 4.6 (± 0.6) | n = 3 |
| Dickite + Malonate | 2.7 (± 0.1) | n = 3 |

# References

1.      Febo, A.; Perrino, C.; Gherardi, M.; Sparapani, R., Evaluation of a High-Purity and High-Stability Continuous Generation System for Nitrous Acid. *Environmental Science & Technology* **1995,** *29* (9), 2390-2395.

2.      Scharko, N. K.; Berke, A. E.; Raff, J. D., Release of Nitrous Acid and Nitrogen Dioxide from Nitrate Photolysis in Acidic Aqueous Solutions. *Environmental Science & Technology* **2014,** *48* (20), 11991-12001.

3.      Thatenhorst, D.; Rheinlaender, J.; Schaffer, T. E.; Dietzel, I. D.; Happel, P., Effect of Sample Slope on Image Formation in Scanning Ion Conductance Microscopy. *Anal Chem* **2014,** *86* (19), 9838-9845.

4.      Bish, D. L.; Johnston, C. T., Rietveld refinement and Fourier-transform infrared spectroscopic study of the dickite structure at low temperature. *Clays Clay Miner.* **1993,** *41* (3), 297-304.

5.      Foster, A. L.; Brown, G. E.; Parks, G. A., X-ray Absorption Fine-Structure Spectroscopy Study of Photocatalyzed, Heterogeneous As(III) Oxidation on Kaolin and Anatase. *Environ. Sci. Technol.* **1998,** *32* (10), 1444-1452.

6.      Bookin, A. S.; Drits, V. A.; Plançon, A.; Tchoubar, C., Stacking Faults in Kaolin-Group Minerals in the Light of Real Structural Features. *Clays Clay Miner.* **1989,** *37* (4), 297-307.

7.      Johnston, C. T.; Kogel, J. E.; Bish, D. L.; Kogure, T.; Murray, H. H., Low-Temperature FTIR Study of Kaolin-Group Minerals. *Clays Clay Miner.* **2008,** *56* (4), 470-485.

8.      Fraser, A. R.; Wilson, M. J.; Roe, M. J.; Shen, Z. Y., Use of hydrofluoric acid dissolution for the concentration of dickite and nacrite from kaolin deposits: an FTIR study. *Clay Miner.* **2002,** *37* (3), 559-570.

9.      Johnston, C. T.; Agnew, S. F.; Bish, D. L., Polarized single-crystal Fourier-transform infrared microscopy of Ouray dickite and Keokuk kaolinite. *Clays Clay Miner.* **1990,** *38* (6), 573-83.

10.     Zbik, M.; Smart, R. S. C., Nanomorphology of Kaolinites: Comparative SEM and AFM Studies. *Clays Clay Miner.* **1998,** *46* (2), 153-160.

11.     Gupta, V.;  Hampton, M. A.;  Nguyen, A. V.; Miller, J. D., Crystal lattice imaging of the silica and alumina faces of kaolinite using atomic force microscopy. *J. Colloid Interface Sci.* **2010,** *352* (1), 75-80.

12.     Siretanu, I.;  van den Ende, D.; Mugele, F., Atomic structure and surface defects at mineral-water interfaces probed by in situ atomic force microscopy. *Nanoscale* **2016,** *8* (15), 8220-8227.

13.     Barron, P. F.;  Frost, R. L.;  Skjemstad, J. O.; Koppi, A. J., Detection of two silicon environments in kaolins by solid-state 29Si NMR. *Nature* **1983,** *302* (5903), 49-50.

14.     Kogure, T.; Inoue, A., Determination of Defect Structures in Kaolin Minerals by High-Resolution Transmission Electron Microscopy (HRTEM). *Am. Mineral.* **2005,** *90* (1), 85-89.

15.     Newman, A. C. D., *Chemistry of clays and clay minerals*. Longman Scientific & Technical: Essex, England, 1987; p 480.

16.     Bruker_AXS *SAINT*, V8.40A (2020); Madison, WI, 2018.

17.     Krause, L.;  Herbst-Irmer, R.;  Sheldrick, G. M.; Stalke, D., Comparison of silver and molybdenum microfocus X-ray sources for single-crystal structure determination. *Journal of Applied Crystallography* **2015,** *48* (1), 3-10.

18.     Sheldrick, G., SHELXT - Integrated space-group and crystal-structure determination. *Acta Crystallographica Section A* **2015,** *71* (1), 3-8.

19.     Sheldrick, G., Crystal structure refinement with SHELXL. *Acta Crystallographica Section C* **2015,** *71* (1), 3-8.

20.     Carter, D. L.;  Campbell, L.;  Rooney, D.;  Clipson, N.; Gleeson, D. B., Specific Surface Area. In *Methods of Soil Analysis. Part 1. Physical and Mineralogical Methods*, Klute, A., Ed. SSSA-ASA: Madison, WI, 1986; pp 413-423.